Journal of
Materials Chemistry C

PAPER

View Article Online
View Journal | View Issue

Cite this: J. Mater. Chem. C, 2016, 4, 11548

Received 23rd August 2016,
Accepted 12th November 2016

DOI: 10.1039/c6tc03648a

www.rsc.org/MaterialsC

Conductive molecularly doped gold films

Hadas Naor, Yiftach Divon, Lior Iagher, Lioz Etgar* and David Avnir*

We describe a general synthesis of conductive gold thin films doped with entrapped organic molecules, and demonstrate, for the first time, the immobilization of a redox couple within an electrode in a single step. The resulting film is of dual properties: conductivity arising from the gold, and redox behavior originating from the entrapped molecule. Faster electron-transfer rates are found for the entrapped case, compared to adsorption. The conductivity of the film affects the organic molecule–metal interactions, as seen in resistivity measurements, in Raman spectroscopy of the metal-entrapped molecules and from a remarkable red shift of 30 nm in emission spectroscopy. Doping is found to affect the work function of gold. Thin conductive doped metal films are of relevance to a variety of applications such as electrochemical detectors, electrode materials for electrochemical impedance spectroscopy, micro and nano electronics interconnects for packaging and for printed circuit boards. The ability to fine-tune the work function opens the possibility to design the desired energy level gaps for optoelectronic applications such as light emitting diodes (LEDs), solar cells and transistors.

Introduction

The development of the new family of molecularly doped metals,[1] molecule@metal, opened the way to prepare many new functional materials, ranging from new catalysts,[2,3] to biomaterials,[4,5] to chiral metals,[6,7] and more.[8,9] Most applications are related to powders, discs and supported nanoparticles,[10] but as many more applications are associated with thin films, we recently began the development of methodologies for the formation of thin films of doped metals.[11,12] This was achieved by focusing on new electroless-based methods which resulted in molecule@Ag[12] and molecule@Au films.[11] The original film morphology obtained for the doped gold films[11] was of disconnected islands, that is, the gold films were non-conductive. Since one of the key features of gold films, which leads to many of their applications, is conductivity, it was clear that this problem must be solved, if applications of these hybrid films are to be developed. Here, we report the successful solution to that problem, and this enables, for instance, the first one-process preparation of a redox-active doped gold film electrode. The transition from non-conductive to conductive doped gold films is of relevance to various applications, including electrochemical detectors for microfabricated electrophoresis chips,[13] electrode materials for electrochemical impedance spectroscopy (EIS),[5,14] micro and nano electronics interconnects for packaging and for printed circuit boards (PCBs),[15,16] and electroconductive textiles.[13,15] We recall that the entrapment within gold described here is a 3D process in which the molecules are surrounded all around by the metal crystallites, held with dipole, pi–pi, van der Waals and simple physical caging interactions, while adsorption is a 2D process where the molecules are arranged on the surface in an orientation which is dictated by a specific moiety of the adsorbed or chemisorbed molecule. 3D entrapment leads therefore to the ability to connect almost any organic molecule to gold, without considering the specific properties of the molecule such as charge or special functional groups. Indeed, in this work three different molecules (Fig. 1) were entrapped within the conductive gold films: the cationic thionin (Th), the anionic bromocresol green (BcG), and the fluorescent rhodamine B (RhB), all resulting in molecule@Au composite films. These three dopants were also selected due to their ability to be used as markers in the different characterization methods described below. We found that as a result of the induced conductivity, the interactions of the

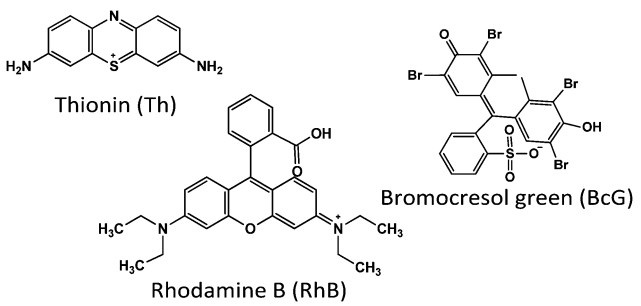

Fig. 1 Molecules entrapped in gold conductive thin films using the metal-doping electroless processes.

Institute of Chemistry and the Center for Nanoscience and Nanotechnology, the Hebrew University of Jerusalem, Jerusalem 91904, Israel.
E-mail: lioz.etgar@mail.huji.ac.il, david.avnir@mail.huji.ac.il

entrapped molecules with the gold have changed compared to the non-conductive case. These changes were detected by Raman spectra from within the films, and by a large red shift in the emission spectrum of RhB.

Experimental details

Chemicals and materials

Thionin acetate (Th), bromocresol green (BcG), rhodamine B (RhB), trisodium citrate tribasic dehydrate (99%), hydroxylamine hydrochloride (98%), poly(diallyldimethylammonium chloride) (PDDA) and gold(III) chloride (99.99%) were purchased from Sigma-Aldrich. The gold chloride was dissolved in a 1 M HCl solution. Glass slides (surface roughness <1 nm rms) were purchased from Schott.

Formation of the doped conductive thin films

The conversion from the disconnected island morphology to the conductive morphology required modification of previous procedures[10,17] as follows. First, colloidal gold was prepared from $HAuCl_4$:[19] 12.5 μL of $HAuCl_4$ 1 M was dissolved in 50 mL triple distilled water (TDW) and heated to boil under stirring; the solution was kept under these conditions until the end of the synthesis. 13 mg sodium citrate was dissolved in 1.25 mL TDW and the solution was added to the boiling gold salt solution. After about a minute a grayish-blue hue appeared, gradually changing into a deep red wine color and the colloid was stored at 4 °C after an additional 5 minutes of boiling. For deposition of the gold particles the glass slides were first cleaned *via* 5 minutes of sonication with ethanol and dried with a nitrogen stream, followed by an ultraviolet ozone cleaning system (UVOCS) for 20 minutes (which can be replaced by cleaning with a piranha solution). The cleaned slides were immersed in 0.01 M PDDA solution for 2 hours, rinsed again with water and dried under a nitrogen stream. The polymer-coated slides were subsequently incubated overnight in the colloidal gold solutions and the AuNP self-assembled on it. The gold layer was rinsed with water and then dried under a nitrogen stream. The improvement of the adhesion and the uniformity of the catalytic layer were achieved by dipping the AuNP-coated slide in an electroless solution containing 3.8 μL of 1.0 M $HAuCl_4$ and 10.0 mL of 0.40 mM hydroxylamine hydrochloride for 15 minutes under agitation. The slide was then taken out from the solution and immediately used for the metal doping process: the slide was dipped again in a fresh electroless solution (3.8 μL of 1.0 M $HAuCl_4$ and 10.0 mL of 0.40 mM hydroxylamine hydrochloride) to which 12.5 μL of 5.0 mM solution of the dopant (each of the three dyes) was added and the slides were then agitated for 60 minutes in that combined solution. It should be noted that this agitation step, along with the formation of the gold-particle catalytic layer, are crucial for obtaining good conductive films; lack of these features results in island morphology. The final doped gold film was then rinsed with water and dried under a nitrogen stream. The film thickness was determined by using the non-erasable pen method.

Comparative surface deposition

Pure gold films were prepared as described above but without the dopant. One drop of the dopant solution (at concentrations of 25 μm (BcG), 5 mM (Th) or 2.65 mM (RhB)) was cast on the gold film and dried.

Cyclic voltammetry measurements

Cyclic voltammograms of free Th molecules in solution and of Th@Au films were carried out using a CHI-630B potentiostat (CH Instruments Inc., TX, U.S.A.) in a conventional three-electrode cell comprising of a composite of the Th@Au film as the working electrode, a platinum wire as the counter electrode, and Ag|AgBr as the reference electrode. Voltammetry was performed at different sweep rates (20, 40, 60, 80, 100 mV s^{-1}) in acetonitrile containing 0.1 M tetrabutylammoniumtetrafluoroborate (TBATFB) as the supporting electrolyte without Th in the solution. A comparative three-electrode cell was carried out with a self-made gold film as the working electrode, prepared similarly but without the Th, and 75 μM free Th in the solution.

Characterization and instrumentation

High resolution scanning electron microscopy (HR-SEM) observations were performed using Sirion (FEI) and Magellan (400 L) microscopes, operating at 5 or 10 kV. Samples were prepared by placing a small piece of glass with a sample on it on a stub with carbon tape. Raman and SERS (surface-enhanced Raman spectroscopy) measurements were taken using a Renishaw InVia Raman microscope with a maximum output of 300 mW at a wavelength of 785 nm for excitation (only 0.0001% power of the laser was used). The Raman microscope includes an objective Leica microscope. The grating for the 785 nm laser is 1200 lines per mm. The electrical resistivity of Au films was measured using an in-line Four Point Probe (Lucas Labs S-302-4). X-ray photoelectron spectroscopy (XPS) measurements were performed on a Kratos Axis Ultra X-ray photoelectron spectrometer. XRD measurements were carried out using a Philips automated powder diffractometer (with a PW1830 generator, PW1710 control unit, PW1820 vertical goniometer, 40 kV, 30 mA, Cu Kα1 (1.5406 Å)). The crystallite size was calculated from the experimental XRD data through the Scherrer equation using the TOPAS v.3 software, including all the observable peaks by averaging the results from all the crystallites in the material. UV-vis absorption spectroscopy was carried out using a Jasco V-630 spectrophotometer. Surface photovoltage spectroscopy (SPS) was performed on a KP technology system model SKP5050-SPS040. Contact potential difference (CPD) between the sample and the vibrating tip was measured using the Kelvin probe technique. Samples were measured in a Faraday cage under an air environment. Before the measurement, the samples were stabilized with a tip for about 30 min. The work function (WF) was calculated according to $WF_{sample} = WF_{tip} - CPD_{(tip-sample)}$. Photoluminescence measurements were performed using an Edinburgh Instruments FLS920 Fluorescence Spectrometer. Samples were excited with monochromatized light from a Xe lamp. The emission was collected at a right

angle, dispersed using a double-monochromator and collected using a Hamamatsu R2658P-PMT.

Results and discussion

Film formation and characterization

SEM and XRD. Typical SEM pictures (Fig. 2) show the compact dense granular morphology for all the doped films – Th@Au, BcG@Au and RhB@Au – in fact, even more compact than the pure gold film, prepared under similar conditions (Fig. 2d). Morphological effects of the type of dopant are seen as well: for instance, RhB (Fig. 2c) induces irregular condensed shapes, less ordered and larger than in Th@Au (Fig. 2a), probably due to the strong interaction between the sulfur group of Th and the forming gold crystal. To gain insight into the building blocks that form the condensed aggregates, X-ray diffraction (XRD) pattern measurements were performed (Fig. 3). Comparison of the three composite molecule@Au with the pure gold film shows that the typical XRD pattern of gold[20] is retained in all cases: $2\theta = 38.2^\circ$, 44.4°, 64.6°, 77.6° and 81.7°, respectively, for Au(111), Au(220), Au(200), Au(311) and Au(222). Notably, although the 2θ value did not vary compared to the fcc bulk gold,[21,22] the crystallographic orientation of the Au(111) crystallographic planes was the preferred growing orientation for this electroless process. The XRD measurements were also used to calculate the average sizes of the elementary building blocks by using Scherrer's equation. These were found to be 16 nm, 25 nm, and 34 nm for the composites Th@Au, BcG@Au, and RhB@Au, respectively, compared with 30 nm for the pure gold film. Interestingly, the larger particle size of RhB@Au also translates to the larger aggregates and to the larger condensed islands of RhB@Au compared to the other films. The fact that Th@Au has the smallest particles is apparently due to the chemical structure of Th (Fig. 1) – it is the only dopant which has sulfur in its structure, an element known for its strong interaction with gold; these interactions slow the growth of the Au particle in this process.

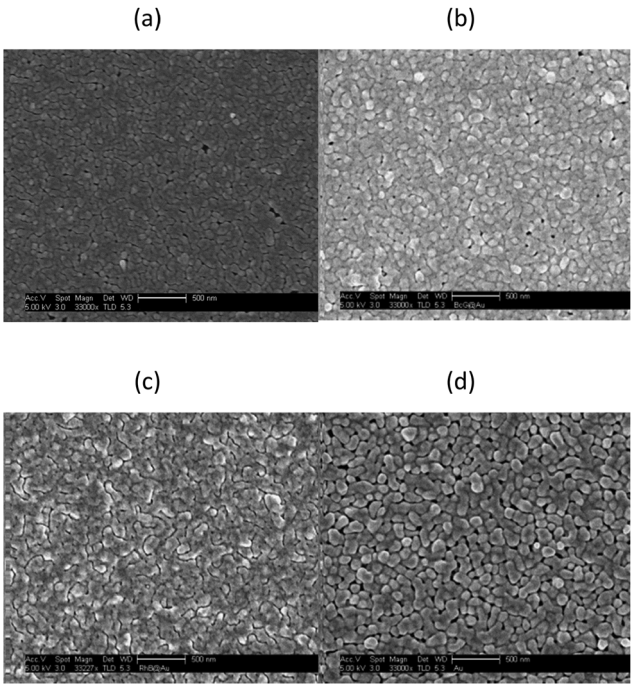

Fig. 2 HR-SEM images of dopant@Au: (a) Th@Au, (b) BcG@Au, (c) RhB@Au, and (d) undoped Au (bars: 500 nm).

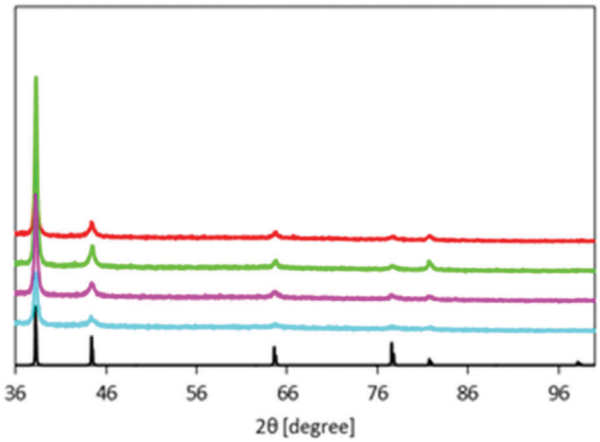

Fig. 3 X-ray diffraction pattern of the composites: Th@Au (blue), BcG@Au (pink), RhB@Au (green) and gold electroless film (red). Literature diffraction data of powdered Au[21] are displayed at the bottom.

Profilometry and film thickness. The film thicknesses were measured using profilometry (Fig. 4), which also provides information about the roughness. The average thicknesses are 120 nm, 176 nm and 166 nm for Th@Au, BcG@Au and RhB@Au, respectively, compared to 293 nm for the pure gold film. We propose that the fact that Th@Au is the thinnest, while pure gold is the thickest, is related to the observation that Th@Au is composed of the smallest elementary building blocks, and the thicker films are composed of larger particles, in the following way: the proposed formation mechanism is – see ref. 1 and 10 – that Au seeds form first, the number of which mainly depends on the concentrations of the gold ions and the reducing agent, which is similar for all the samples, and then physisorption of the dopant molecules on these seeds starts the entrapment process and dictates also the size of the forming crystallites. Thus, assuming similarity in the number of initial Au seeds and therefore also in the number of deposited particles for all cases, means that smaller particles will form thinner layers: comparing the deposition processes for the same deposition time (60 minutes) results in thinner films for Th@Au, compared with Au. An important feature in all profiles is the continuity in the rough regions of the profiles which are on top of the continuous catalytic layer – these give rise to the conductivity (described below).

We recall that in the gold electroless process, the reduction of the gold cation involves two steps: first, Au(III) is reduced to Au(I) by hydroxylamine which is oxidized to a nitrite anion;[23] and second, the nitrite continues to reduce the Au(I) to Au^0:

$$2Au^{3+} + NH_2OH + H_2O \rightarrow NO_2^- + 2Au^+ + 5H^+ \qquad (I)$$

$$Au^+ + NO_2^- + H_2O \rightarrow Au^0\downarrow + NO_3^- + H^+. \qquad (II)$$

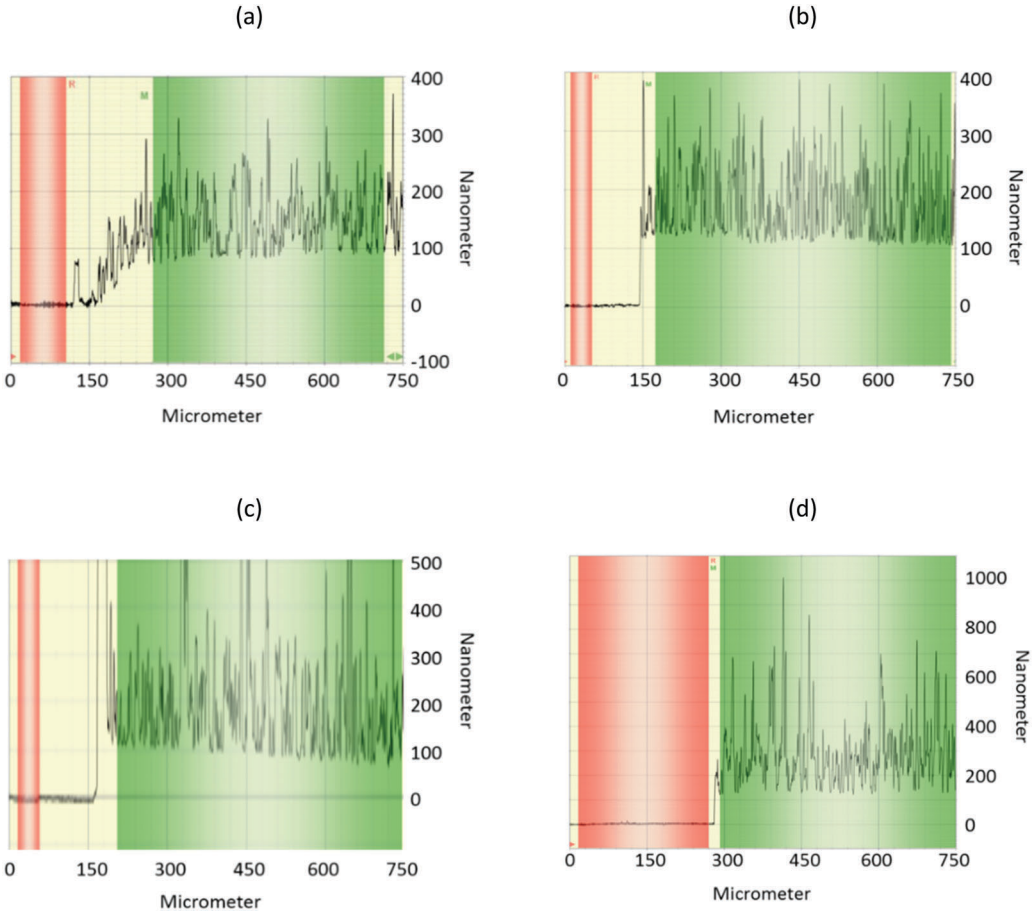

Fig. 4 Film thickness profiles of (a) Th@Au, (b) BcG@Au, (c) RhB@Au, and (d) pure gold (note the different thickness scale).

The entrapment takes place mainly during the second step and the initial aggregation of the resulting Au.[1,10] Fig. 5 shows a typical spectral follow-up of the doping electroless process for Th@Au. The disappearance of the gold cation (Fig. 5a) and of Th (Fig. 5b) from the supernatant solution is clearly seen. It is also seen (Fig. 5a) that the presence of the Th molecules slows down the reduction of the gold cation, an effect that reflects the complexation of the latter through the heteroatoms of Th.

The organic dopants: Raman spectroscopy

Over the last 50 years, Raman spectroscopy has been used as a powerful tool to detect and identify the interaction between organic molecules and metal surfaces, notably gold and silver,[24] due to the high enhancement of the molecule's Raman scattering by interaction with the metal surface plasmons (surface-enhanced Raman spectroscopy – SERS). One of the main results of the ability to dope metallic thin films using the methodology described here is the ability to get spectral information on the dopant from within a 3D metallic cage,[10,11,25] and to prove directly that entrapment has occurred. We begin with the SERS spectrum of Th@Au and compare it to the Raman spectrum of Th adsorbed on a pure gold film (Fig. 6a). The two processes lead to completely different metal–molecule interactions: while in a 2D adsorption process the molecules interact with the metal surface mainly through a specific moiety, in a 3D entrapment process the molecules within the cages involve a variety of interactions of all of the functional groups with the gold. Changes can therefore be seen in the SERS spectra of entrapment *vs.* adsorption. The first striking change is that the enhancement factor in the entrapped case is four orders of magnitude larger (!) compared to adsorption even though the concentration of the latter is higher. One is witnessing here the known roughness effect on the level of enhancement – the rougher the surface is, the higher is the enhancement.[26] As explained before,[12] using fractal-dimensions terminology, the rougher the surface is, the higher is its effective dimension; in the extreme case of a surface which fills a volume such as in 3D-crumpling, the surface is so rough that its effective dimension is very close to three.[27] The second change observed between these two systems is revealed when the two spectra are normalized for their different intensities (Fig. 6b): it is seen that while the two spectra seem to be overall similar to each other, variations can be observed, which originate from the differences between the molecule–metal interactions in entrapment compared to adsorption:[12] it is seen that while in the adsorbed case, the low wavenumber range of up to 900 cm^{-1} reveals clearly various skeletal deformation modes,[28] fewer and less pronounced peaks are seen for the entrapped case. This is seen, for instance, for the

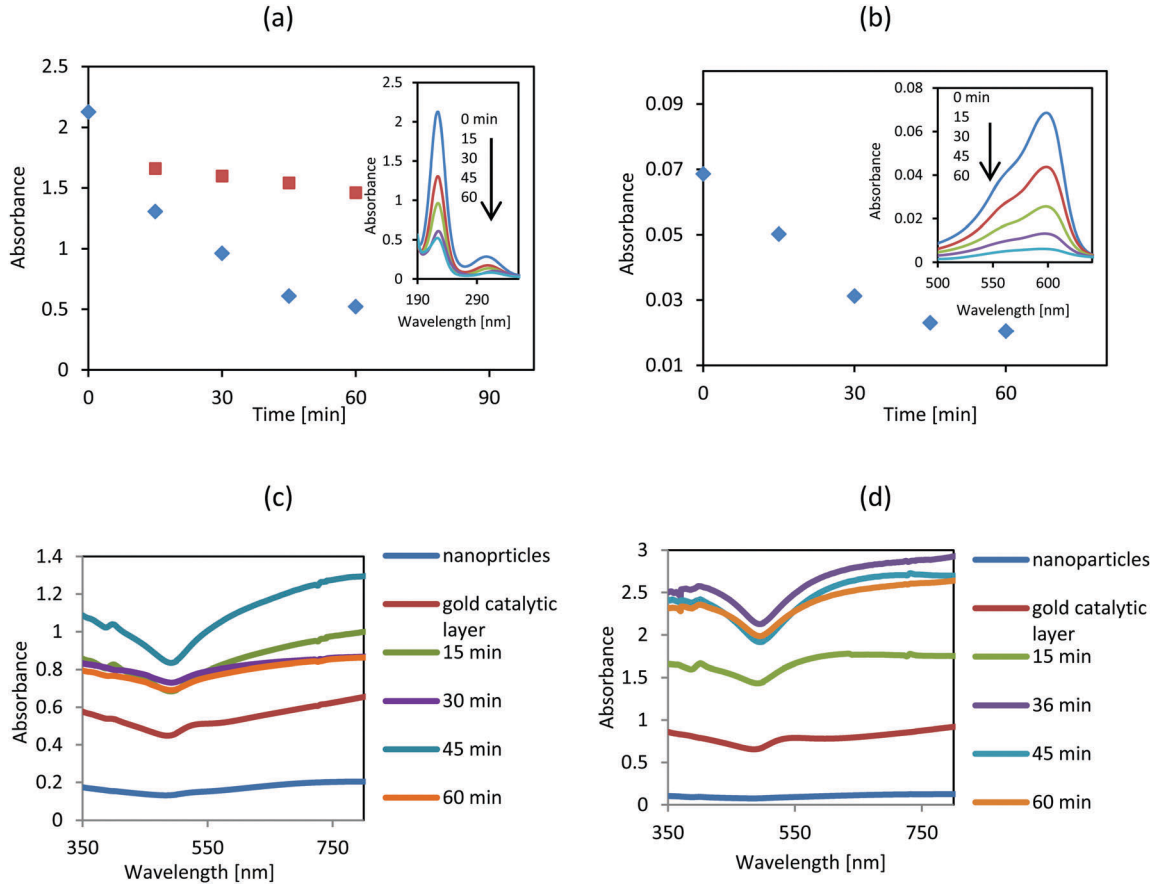

Fig. 5 (a) The disappearance kinetics of the gold ions from the electroless supernatant solution during the formation of Th@Au ■ compared to pure gold ◆ (see also the inset), monitored at a wavelength of 224 nm. (b) The disappearance kinetics of thionin (see also the inset) monitored at 599 nm. (c) The changes in the UV-vis absorption spectra of the films during the formation of Th@Au and (d) pure gold.

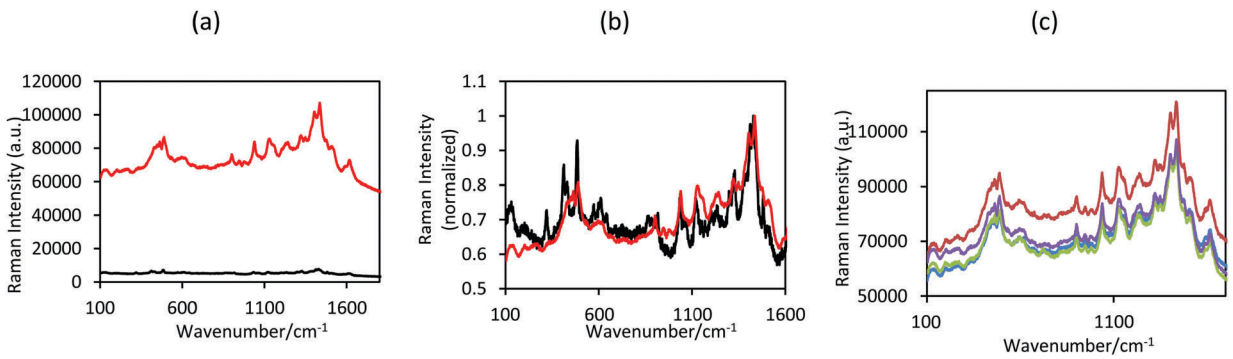

Fig. 6 Enhanced Raman spectra of thionin: (a) Th@Au (red; 0.0001% power of the laser) compared to Th adsorbed on the gold electroless layer (black; 0.05% power of the laser). (b) The normalized intensity spectra of (a). (c) Spectra of Th@Au taken from four different points of the film.

peak at 317 cm^{-1} and for the doublet at 411 and 429 cm^{-1}, which are assigned (following Hutchinson *et al.*[28]) to the NH_3 torsion mode and to the skeletal deformation of C–N–C and C–C–C bending, respectively. The peaks with wavenumbers higher than 900 cm^{-1} originate mainly from various stretching modes and in-plane bending, and the main feature is of broadening in the entrapped case compared to adsorption. This can be seen, for instance, in the C–H out-of-plane bending[29] peak at 1129 cm^{-1} and in the stretching vibration at 1240 cm^{-1} of the entrapped spectrum. Note also the C–N asymmetric stretching band doublet at 1412 and 1429 cm^{-1} (adsorption), attributed to the strong bond of the amino group of Th with the gold surface,[29] which is shifted to 1406 and 1436 cm^{-1} (entrapment). Fig. 6c provides an important observation: spectra taken from four different points in the film are very similar to each other. This is an indication of the homogeneity of the film, and of the fact that the surrounding

cages around the entrapped molecules are repetitive. In the previously reported non-conductive island morphology, this homogeneity could not be achieved, and the spectra varied from one point to the other.[11]

Next, we briefly comment on the SERS spectra of BcG@Au (Fig. 7) and of RhB@Au (Fig. 8). The enhancement in the Raman signal of the entrapped case compared to the adsorbed case which we have seen for Th@Au is not seen here – apparently the much smaller crystallite sizes of the gold in the case of Th@Au compared to the other films (see above), and the strong interaction of the sulfur group of Th with the gold, which is absent in the other dopants, are responsible for that difference in behavior. The fact that the SERS of BcG could be obtained at all is special, because unlike thionin (and RhB), BcG molecules are negatively charged and therefore it is practically very difficult to adsorb these molecules on gold, which itself is negatively charged when stabilized by citrate and other anionic ligands. In fact, only entrapment opens the possibility of combining BcG and gold together. As seen in Fig. 7a, this film too is quite homogeneous – spectra taken from three different points are very similar to each other. The only comparison that could be carried out is to dry a solution of BcG on a pure gold electroless layer, thus obtaining crystalline BcG in touch with gold (Fig. 7b). Shifts are again seen – for instance the band at 1576 cm^{-1} which corresponds to the C–C bond vibration in the aromatic ring[30] (adsorption) moves to 1582 cm^{-1} (entrapment); and broadenings are seen again, such as the broadening of the 1342 cm^{-1} peak (of the sulfonate group) in the entrapped case, compared to the 1390 cm^{-1} band in the adsorbed case. In the case of BcG, another analytical method could be used reliably for direct detection of the dopant, namely X-ray photoelectron spectroscopy (XPS), because of the existence of Br atoms in the molecule. This method provides information about the elemental composition to a depth of a few nanometers, thus giving additional direct confirmation of the existence of the organic molecules in the gold film. Analyzing the signal ratios of the marker four bromine atoms (Br 3d 5/2 peak – 68.3 eV, Br 3d 3/2 peak – 69.3 eV) and the gold (Au 4f 7/2 peak – 84.1 eV, Au 4f 5/2 peak – 87.8 eV) in the BcG@Au composite, a loading of 1.1 mol% was detected, which agrees very well with the inserted electroless solution loading of 1.0 mol% of the dopant molecules during the synthesis (taking into account the gold catalytic layer).

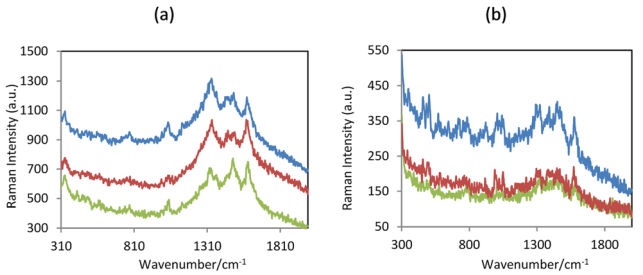

Fig. 7 Enhanced Raman spectra of (a) BcG@Au and (b) of BcG solution dried on a pure gold electroless layer.

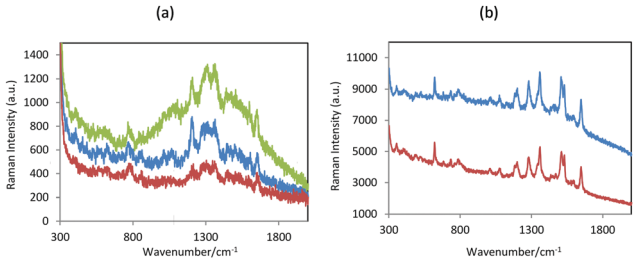

Fig. 8 Enhanced Raman spectra of (a) RhB@Au (0.1% power of the laser) and (b) drop of RhB solution dried on a pure gold electroless layer (0.001% power of the laser).

Finally, the SERS properties of the entrapped RhB (selected because of its fluorescence properties – see Conclusion and outlook) were determined, and are shown in Fig. 8, again displaying good reproducibility (Fig. 8a) and differences between entrapped molecules and adsorbed ones (Fig. 8b). For instance, note that the C–C bridge stretching mode at 1281 cm^{-1} (following Wang *et al.*[24]) in the adsorbed case is broadened and shifted in the entrapped case to 1307 cm^{-1}; that the aromatic ring flexural vibration at 622 cm^{-1} in the adsorbed case disappears in entrapment, and *vice versa*, that the small peak of the C–N stretching vibration at 1441 cm^{-1} in the entrapped case disappears from the adsorbed spectrum.

Conductivity and work function

As described in the Introduction, the main goal of this study was to preserve the conductivity of the gold film even while inserting dopant molecules, in order to open the door for applications which rely on that property. The conductivity goal has not been trivial because of the interference of the dopant with the electroless process, which, indeed, resulted in an earlier study in non-conductive disconnected island film morphology.[11] The procedure, described in the Experimental details section, was obtained after extensive optimization solved this challenge; while repeating this procedure one should pay attention to details such as agitation of the electroless plate to accelerate the kinetics of the electroless process,[18] and the formation of a good pure gold catalytic layer needed for stable adhesion properties of the gold film to the substrate. We found that the resulting films so obtained retained the conductivity of gold with no major effect of the dopant. The resistivity values were 0.76 $\Omega\ sq^{-1}$ for BcG@Au and 0.63 $\Omega\ sq^{-1}$ for RhB@Au, compared with 0.82 $\Omega\ sq^{-1}$ for the pure Au film (Th@Au is too thin to be measured reliably). In fact since these values are from 3–4 repetitions of measurements, we believe that the slightly better conductivity in the presence of the dopants is authentic. The reason for this observation is not clear to us, except that when one carefully observes the pictures in Fig. 4, it is seen that the pure Au film has more disconnection points, and that the doped films are much more homogeneous from that point of view – again, apparently an effect of the smaller elementary particle sizes in the doped films.

Preserving the conductivity has enabled us to measure, for the first time, the work function of these composites and to

Table 1 Work functions of the doped films

Sample	WF (eV)
Au	5.00
Th@Au	5.12
RhB@Au	5.03
BcG@Au	5.13

determine how the dopants affect the work function of the entrapping metal. The values – collected in Table 1 – demonstrate that organically doping opens the way to control and fine-tune the work function of metals. Currently, the main method for such control is by adsorbing self-assembled polar molecules on the metal surface.[31–33] Doping provides numerous advantages that have already been demonstrated in previous studies:[1] the molecules cannot be easily washed away as in adsorption; the entrapped molecule enjoys a much better stability and protection from harsh environmental conditions; molecules which cannot be adsorbed are easily entrapped; much higher concentrations of the organic molecule are obtained by 3D doping, compared with 2D adsorption; and the doped metallic film offers better compliance with device construction restrictions.

Electrochemistry and the redox-couple

For the redox-couple behavior characterization we focused on Th, which has been a classic redox indicator in similar studies.[28,34] Cyclic voltammetry was performed on Th from within the gold cages and compared with free Th in solution. Fig. 9 shows the cyclic voltammograms of two different gold films used as the working electrodes: the composite Th@Au film (Fig. 9a) and the pure gold film prepared by the same procedure (Fig. 9b) in acetonitrile/TBATFB, compared to an Ag|AgBr electrode. When conducting the experiment with the gold electrode, Th was added to the solution (see also Experimental details). The cyclic voltammetry was carried out in a potential window between 1.5 and 0.0 V, using different scan rates of 20, 40, 60, 80 and 100 mV s^{-1}. It is seen (insets of Fig. 9) that the curves of the anodic peak current *vs.* the square root of the scan rate fit very well a linear correlation with the same slope for both systems −0.043 (mA $(s\ mV^{-1})^{0.5}$) – which suggests that the electron transfer process is diffusion-controlled. Furthermore, similar values of the slopes indicate that the Th molecule was unaffected by the entrapment process, and specifically, that there was no strong effect on the ring nitrogen atom, that is, the oxidation–reduction reaction (Fig. 9, top) was not influenced by the entrapment. Moving to the voltammograms of the two systems, they appear overall to be similar. However, careful analysis shows that for the same scan rate, the redox potentials are shifted between the two systems. For instance, at 20 mV s^{-1}, Th in solution showed an anodic peak at −0.60 V and a cathodic peak at −1.06 V with a ΔE_p value of 0.46 V, while entrapment induced a negative shift to −0.65 V in the oxidation peak, and a positive shift to −0.97 V, with a decrease in the ΔE_p value to 0.34 V. Such a decrease in the ΔE_p value means that for Th@Au the electron transfer is faster compared to free Th in solution – a clear outcome of a cage effect in the case of entrapment[35] with a similar tendency seen for Th adsorbed on gold nanoparticles.[36]

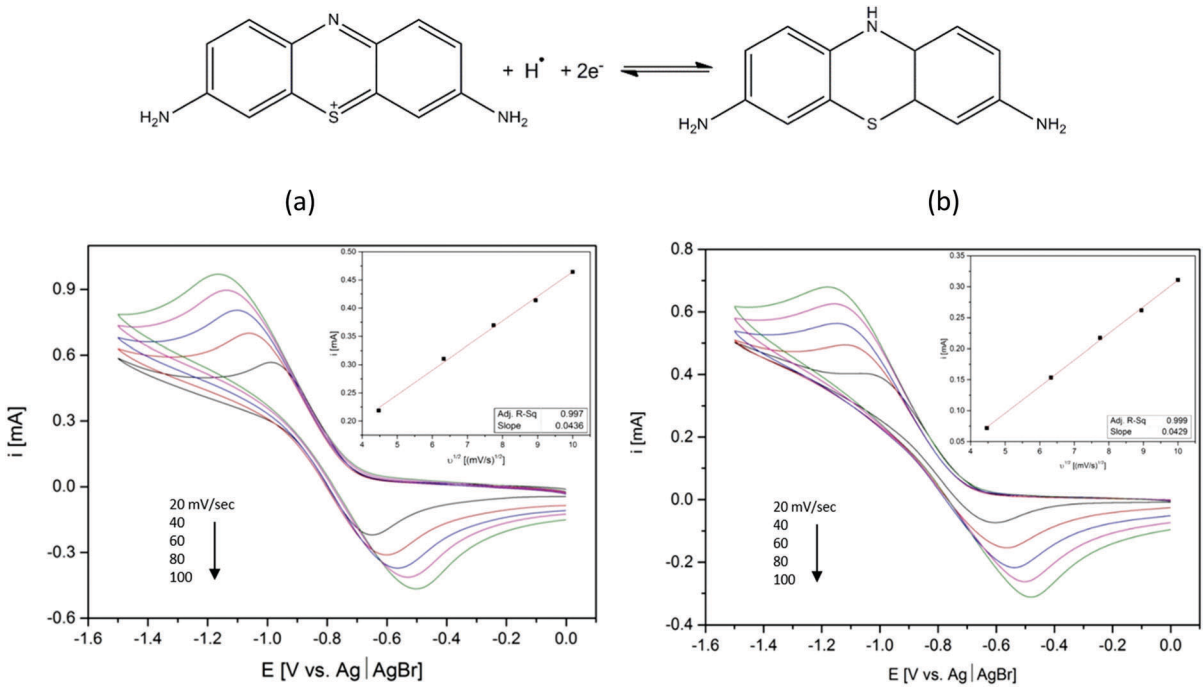

Fig. 9 Top: The redox forms of thionin. Bottom: Cyclic voltammograms of (a) Th@Au against Ag|AgBr in acetonitrile/TBATFB, and (b) thionin in solution using a pure gold electrode. Voltage sweeping rates of 20, 40, 60, 80 and 100 mV s^{-1}. The insets show the plots of the anodic peak current *vs.* the square root of the sweep rate.

Conclusions and outlook

We have developed an electroless methodology for incorporating organic molecules within conductive gold thin films. The typical dopants entrapped in this article represent the large library of organic molecules that can be incorporated into gold films, taking into account that the dopant properties influence the morphology and the properties of the resulting film. The non-trivial combination of entrapment of guest molecules within the gold film without hampering the conductivity properties of the film unravels the potential to use this film in electrochemical measurements. The concept of one synthesis producing a metallic–organic hybrid electrode may be an alternative strategy for the methods used today for surface modification of electrodes, such as the use of spacer bi-functional adsorbates[37] and the utilization of layer by layer methods.[38] This approach can save time, eliminate the need for bi-functional reagents, removing the requirement for an additional mediator to the analyzed solution[39] and enhancing the sensitivity of the electrode due to faster electron transfer. We showed the principle of affecting and fine-tuning the metal's work function; this is one of the most desired abilities in the field of optoelectronics and energy conversion – the full potential of this observation will be explored in our labs.

An interesting outlook of the observation that by the methods described here, the Raman spectra of molecules from within the metal can be recorded, is to explore other spectroscopic methods aimed at the dopant. This, in fact, has been the motivation in preparing RhB@Ag – would it be possible to observe the fluorescence of the dopant? Two preliminary observations, shown in Fig. 10, indicate that this is a direction worth taking: first, the emission of RhB from within the metal is strong and observable making it indeed a second method – in addition to SERS – of obtaining spectral information from a molecule embedded within a metal. It should be noted that in some specific cases, for example for fluorophores that are localized inside gold nanoshells, the excitation field can interact with the molecules' dipole and the brightness is kept.[40] The second observation is that the entrapment in the conductive film causes a major red shift (compared to non-conductive films). This observation indicates that the combination of entrapment and conductivity of the layer allows a smaller energy gap between the ground state and the excitation state and probably relate to coupling of plasmons with fluorescence properties at short interaction distances.[41] Work expanding these preliminary observations into a full report is in progress. Last but not least, an additional optional development for this hybrid film methodology is to prepare thin films of enzyme@metal, so far known only in powder morphologies,[4] for applications such as biosensors, biomedical devices and enzymatic bioreactors.[38]

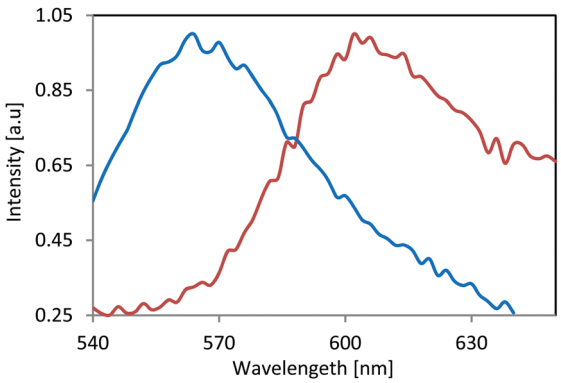

Fig. 10 Emission spectra of RhB@Au films. Red: entrapment in the conductive gold film reported here. Blue: entrapment in the non-conductive gold island film reported in ref. 10.

Acknowledgements

This work was supported by the Israel Science Foundation (grant no. 703/12) and by the FTA program of the Israel Ministry of Commerce and Industry. Special thanks are due to Dr Anna Radko, Ms Evgenia Blayvas and the staff at the Center of Nanoscience and Nanotechnology at the Hebrew University. Useful discussions were carried out with Prof. Daniel Mandler of the Hebrew University of Jerusalem and his graduate student Efrat Gdor.

References

1 D. Avnir, *Acc. Chem. Res.*, 2014, **47**, 579–592.
2 L. Shapiro, M. Driess and D. Avnir, *ChemCatChem*, 2015, **7**, 2033–2037.
3 I. Yosef, R. Abu-Reziq and D. Avnir, *J. Am. Chem. Soc.*, 2008, **130**, 11880–11882.
4 R. Ben-knaz and D. Avnir, *Biomaterials*, 2009, **30**, 1263–1267.
5 R. Ben-Knaz, R. Pedahzur and D. Avnir, *RSC Adv.*, 2013, **3**, 8009–8015.
6 H. Yang, D. Chi, Q. Sun, W. Sun, H. Wang and J. Lu, *Chem. Commun.*, 2014, **50**, 8868.
7 L. Durán Pachón, I. Yosef, T. Z. Markus, R. Naaman, D. Avnir and G. Rothenberg, *Nat. Chem.*, 2009, **1**, 160–164.
8 Y. Ben-Efraim and D. Avnir, *Acta Mater.*, 2013, **61**, 7384–7391.
9 L. Chen, I. Polishchuk, E. Weber, A. N. Fitch and B. Pokroy, *Cryst. Growth Des.*, 2016, **16**, 2972–2978.
10 Y. Aouat, Y. Azan, G. Marom and D. Avnir, *Sci. Adv. Mater.*, 2013, **5**, 598–605.
11 H. Naor and D. Avnir, *J. Mater. Chem. C*, 2014, **2**, 7768–7775.
12 H. Naor and D. Avnir, *ACS Appl. Mater. Interfaces*, 2015, **7**, 26461–26469.
13 A. Hilmi and J. H. T. Luong, *Anal. Chem.*, 2000, **72**, 4677–4682.
14 A. Schwarz, J. Hakuzimana, A. Kaczynska, J. Banaszczyk, P. Westbroek, E. McAdams, G. Moody, Y. Chronis, G. Priniotakis, G. De Mey, D. Tseles and L. Van Langenhove, *Surf. Coat. Technol.*, 2010, **204**, 1412–1418.
15 Y. Kong, H. Chen, Y. Wang and S. A. Soper, *Electrophoresis*, 2006, **27**, 2940–2950.
16 Y. Shacham-Diamand, T. Osaka, Y. Okinaka, A. Sugiyama and V. Dubin, *Microelectron. Eng.*, 2015, **132**, 35–45.

17 Y. Okinaka and M. Hoshino, *Gold Bull.*, 1998, **31**, 3–13.
18 S. Hrapovic, Y. Liu, G. Enright, F. Bensebaa and J. H. T. Luong, *Langmuir*, 2003, **19**, 3958–3965.
19 J. Turkevich, P. C. Stevenson and J. Hillier, *Discuss. Faraday Soc.*, 1951, **11**, 55–75.
20 J. Hu, W. Li, J. Chen, X. Zhang and X. Zhao, *Surf. Coat. Technol.*, 2008, **202**, 2922–2926.
21 ICDD – Card no. 01-071-4073.
22 I. K. Suh, H. Ohta and Y. Waseda, *J. Mater. Sci.*, 1988, **23**, 757–760.
23 R. C. Prince and G. N. George, *Nat. Struct. Biol.*, 1997, **4**, 247–250.
24 W. Wang, W. Li, J. Ye and R. Zhang, *J. Polym. Mater.*, 2010, **27**, 351–357.
25 S. Hou, J. Yan, Z. Hu and X. Wu, *Chem. Commun.*, 2016, **52**, 3–6.
26 M. L. Tseng, C. M. Chang, B. H. Cheng, P. C. Wu, K. S. Chung, M.-K. Hsiao, H. W. Huang, D.-W. Huang, H.-P. Chiang, P. T. Leung and D. P. Tsai, *Opt. Express*, 2013, **21**, 24460–24467.
27 D. Farin, A. Volpert and D. Avnir, *J. Am. Chem. Soc.*, 1985, **107**, 3368–3370.
28 K. Hutchinson, R. E. Hester, W. J. Albery and A. R. Hillman, *J. Chem. Soc., Faraday Trans. 1*, 1984, **80**, 2053–2071.
29 Y. Yuan, L. Ling, X. Wang, M. Wang, R. Gu and J. Yao, *J. Raman Spectrosc.*, 2007, **38**, 1280–1287.
30 W. Zhang and S. R. P. Silva, *Carbon*, 2010, **48**, 2063–2071.
31 B. De Boer, A. Hadipour, M. M. Mandoc, T. Van Woudenbergh and P. W. M. Blom, *Adv. Mater.*, 2005, **17**, 621–625.
32 J. P. Hong, A. Y. Park, S. Lee, J. Kang, N. Shin and D. Y. Yoon, *Appl. Phys. Lett.*, 2008, **92**, 20–23.
33 S. Osella, D. Cornil and J. Cornil, *Phys. Chem. Chem. Phys.*, 2014, **16**, 2866–2873.
34 C. Dohno, E. D. A. Stemp and J. K. Barton, *J. Am. Chem. Soc.*, 2003, **125**, 9586–9587.
35 C. R. Raj, T. Okajima and T. Ohsaka, *J. Electroanal. Chem.*, 2003, **543**, 127–133.
36 Y. Ding, X. Zhang, X. Liu and R. Guo, *Langmuir*, 2006, **22**, 2292–2298.
37 D. D. Schlereth, E. Katz and H.-L. Schmidt, *Electroanalysis*, 1995, **7**, 46–54.
38 Y. M. Lvov, Z. Lu, J. B. Schenkman, X. Zu and J. F. Rusling, *J. Am. Chem. Soc.*, 1998, **120**, 4073–4080.
39 S. Liu, D. Leech and H. Ju, *Anal. Lett.*, 2007, **36**, 37–41.
40 S. Zaiba, F. Lerouge, A. M. Gabudean, M. Focsan, J. Lermé, T. Gallavardin, O. Maury, C. Andraud, S. Parola and P. L. Baldeck, *Nano Lett.*, 2011, **11**, 2043–2047.
41 A. Picot, F. Malvolti, B. Le Guennic, P. L. Baldeck, J. a G. Williams, C. Andraud and O. Maury, *Inorg. Chem.*, 2007, **46**, 2659–2665.

